Atmospheric Research 320 (2025) 108033

Contents lists available at ScienceDirect

Atmospheric Research

journal homepage: www.elsevier.com/locate/atmosres

Terrain and urban impacts on summer extreme precipitation over Henan, China: A synoptic and simulation analysis

Shuang Chen [a], Ben Yang [a,*], Anning Huang [a,c,**], Yan Zhang [b]

[a] School of Atmospheric Sciences, Nanjing University, Nanjing 210023, China
[b] Key Laboratory of Radiometric Calibration and Validation for Environmental Satellites, National Satellite Meteorological Center, China Meteorological Administration (LRCVES/CMA), FengYun Meteorological Satellite Innovation Center (FY-MSIC), Beijing 100081, China
[c] Qinghai Lake Comprehensive Observation Research Station, Chinese Academy of Sciences, Gangcha 812300, China

ARTICLE INFO

Keywords:
Regional hourly extreme precipitation
Terrain
Urban
Moisture budget

ABSTRACT

The impacts of terrain and urban surfaces on regional hourly extreme precipitation events (RHEPE) in Henan Province of China under specific synoptic conditions remain unclear. In this study, we first identify the dominant synoptic patterns associated with the summer RHEPEs in Henan and surrounding areas by employing spectral clustering methods, revealing that 86 % of RHEPEs are induced by the low vortexes and 14 % by the tropical cyclones, with the latter contributing to the most extreme RHEPEs. Then, based on numerical experiments and moisture budget decomposition, we quantify the effects of terrain and urban surfaces on RHEPE under the most extreme synoptic pattern featured by tropical cyclones. Results suggest that the terrains cause remarkable increases in precipitation primarily along the windward slopes of the Funiu Mountains and Taihang Mountains by 34 % and 26 %, respectively, this can be explained by the enhanced dynamical component of moisture convergence due to the blocking effect of terrains. Compared to the terrain, the impacts of urban surfaces are much smaller (only 1 %) and spatially limited. The much larger surface roughness in the urban areas reduces the horizontal wind speed and causes weakened wind convergence, leading to decreased precipitation over the urban areas. Meanwhile, when traversing the urban areas, the horizontal winds bifurcating and rejoining in the downwind areas increase the low-level convergence and precipitation there. Findings of this study may deepen our understanding of the influences of terrain and urban surfaces on the RHEPE and associated mechanisms under the extreme synoptic pattern.

1. Introduction

Extreme precipitation (EP) events are widely recognized as major triggers for flash floods and urban waterlogging, with significant impacts on the global society and economy (Tewari et al., 2004; Waliser and Guan, 2017). Under global warming, the intensity and probability of EP events in China have increased remarkably (Huang et al., 2021; Li et al., 2022; Yao et al., 2022). Henan Province of China is a densely populated, food-rich region experiencing increasingly severe EP events (Ding, 2015), with the hourly EP in summer accounting for a considerable proportion of the total summer precipitation (Fig. S1a). During 17–22 July 2021, a historic EP event occurred in Henan, China and the hourly rainfall peak in Zhengzhou (i.e., the capital of Henan) station reached an unprecedented amount of 201.9 mm (Wang et al., 2022). This event resulted in 398 deaths and caused direct economic losses of 120.06 billion RMB (Ma et al., 2023; Zhang et al., 2023). Therefore, understanding the underlying mechanisms of EP in Henan has broad implications for preventing and mitigating future crises.

Previous research has demonstrated that synoptic patterns influence the formation and development of EP events through mechanisms such as modulating atmospheric moisture, instability, and dynamic lifting mechanisms (Tang et al., 2021; Utsumi et al., 2017; Zeng et al., 2023). For instance, tropical cyclones, often classified as a typical synoptic pattern, transport large amounts of moisture from oceanic sources into continental areas, leading to intense precipitation through strong convergence and uplift (Luo et al., 2016). Surface frontal systems similarly promote EP by generating sharp gradients in temperature and humidity, creating an environment conducive to sustained convective

* Corresponding author.
** Corresponding author at: School of Atmospheric Sciences, Nanjing University, Nanjing 210023, China.
E-mail addresses: benyang@nju.edu.cn (B. Yang), anhuang@nju.edu.cn (A. Huang).

https://doi.org/10.1016/j.atmosres.2025.108033
Received 23 December 2024; Received in revised form 27 February 2025; Accepted 1 March 2025
Available online 7 March 2025
0169-8095/

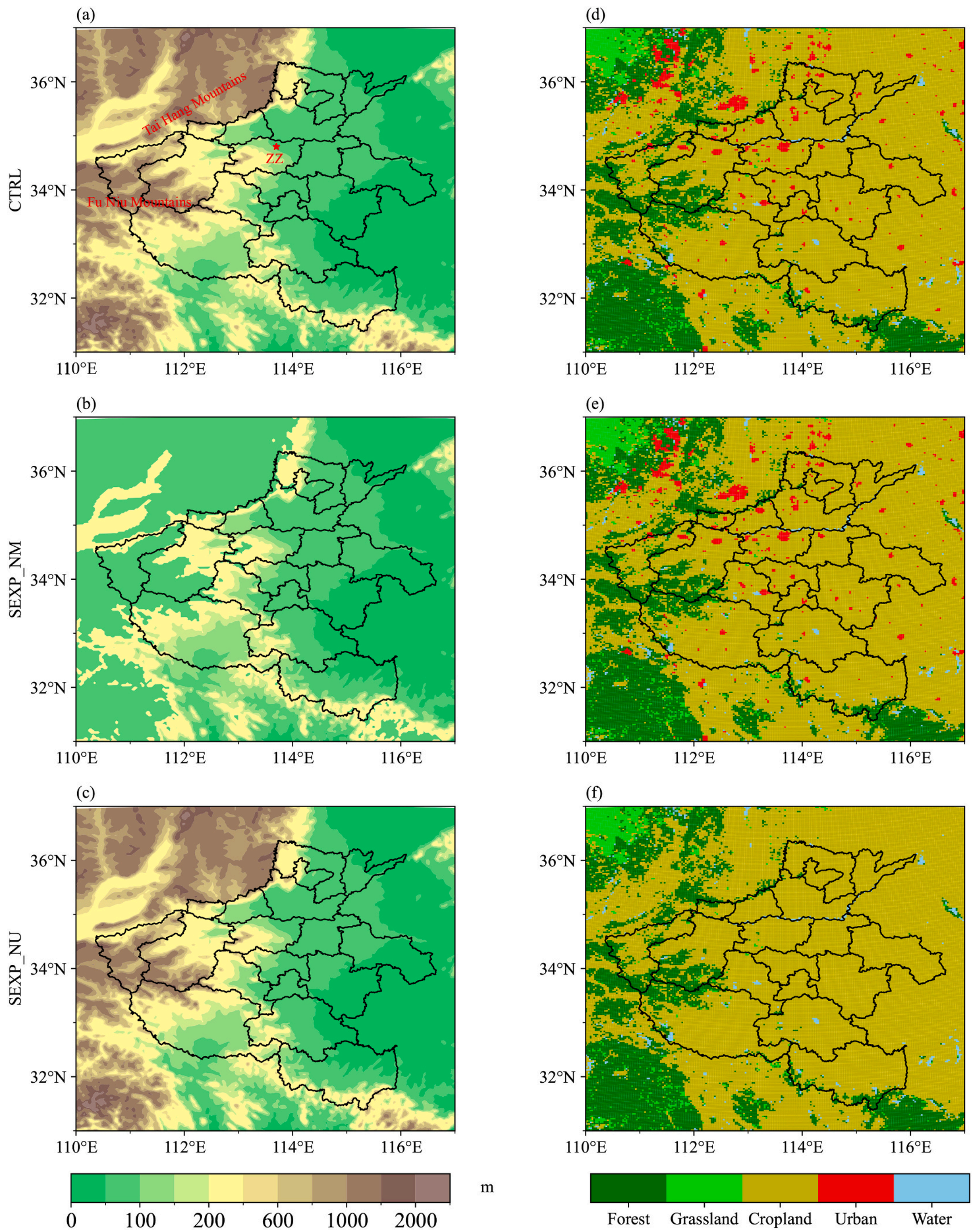

Fig. 1. Terrain height (a–c) and land cover types (d-f) in each experiment. An asterisk indicates the main urban area of Zhengzhou.

activity (Zeng et al., 2023; Zhang et al., 2023; Zhang et al., 2024). Studies such as Tang et al. (2021) have shown that the Meiyu front, quasi-stationary front, and low vortex systems act as dominant mechanisms for EP in eastern China, enhancing rainfall by stabilizing moisture-laden air masses and intensifying vertical motion. Furthermore, Liu et al. (2022) found that the westerly trough induces ascending motion and causes continuous heavy precipitation over northern China through dynamic uplift associated with the upper-level jet stream. Similarly, Zhou et al. (2020) categorized heavy rainfall events in North China into meridional and latitudinal types, where the meridional mode is related to the inflow and vertical movement of water vapor caused by strong low-level southwesterly winds, while the latitudinal mode is related to the convergence of water vapor on the south side of the western Pacific subtropical high. Together, these synoptic patterns shape EP events by altering atmospheric conditions in ways that favor convection and moisture recycling.

In addition to synoptic conditions, local factors such as terrain and the changes in land use/cover can also significantly affect the intensity and distribution of EP (Changnon, 1992; Freitag et al., 2018; Ma et al., 2024; Waliser and Guan, 2017; Yan et al., 2016). Strong precipitation event often occurs along the windward sides of terrains due to the terrain-following uplift and the enhanced vertical moisture transport (Fairman Jr. et al., 2011; Rotunno and Houze, 2007; Sato, 2013). The low-level jets forced by large terrains also tend to intensify the horizontal moisture transport which is essential for the initiation and development of convection (Galewsky and Sobel, 2005; Houze, 2012; Neiman et al., 2002). The Funiu Mountains in the west and the Taihang Mountains in the north of Henan Province have been found to greatly

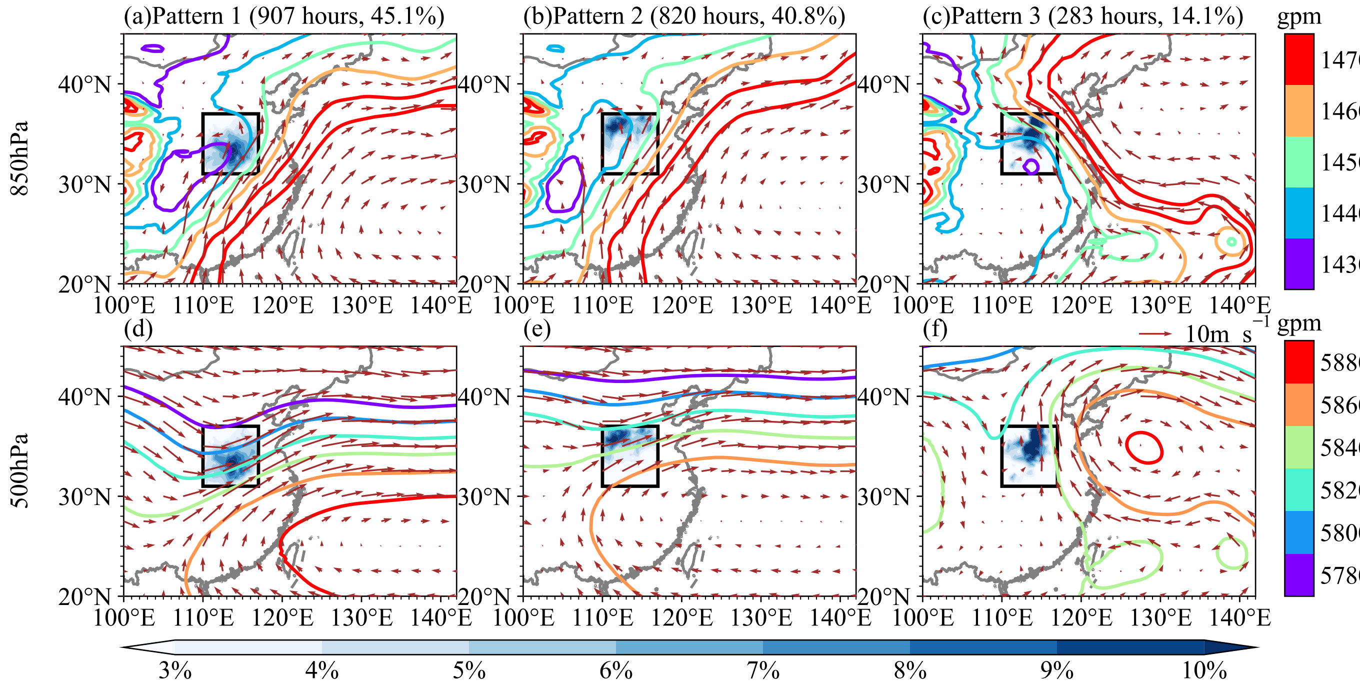

Fig. 2. The composite mean geopotential height (contours) and horizontal wind field (vectors) at 850 hPa (a-c) and 500 hPa (d-f) under synoptic pattern 1 (1st column), 2 (2nd column), and 3 (3rd column) responsible for the summer RHEPEs over Henan and surrounding areas during 1980–2021. The number and frequency of occurrence for each synoptic pattern are shown above in (a-c). The shadings in (a-f) indicate the occurrence probability of EP at each station during RHEPE under each synoptic pattern.

contribute to the EP (Zhao et al., 2020b). For instance, the terrain-induced low-level jet leads to the localized intensification of heavy precipitation in Henan (Li et al., 2023). The moist air originating from tropical cyclones can be transported by southeastern winds to Henan and lifted due to the orographic obstruction of mountains there, amplifying the intensity of EP (Gao et al., 2022b). In addition, the mountain-plain thermal contrast caused by the temperature difference between the mountain cold pool and the warm air flow in the plain planetary boundary layer (PBL) will affect the low-level convergence and thus affect precipitation (Davis and Lee, 2012; Tai et al., 2020; Xu et al., 2012; Zhang et al., 2021).

Urbanization is another important local factor influencing precipitation. For instance, the urban heat island (UHI) effect can cause low-level convergence and high-level divergence, thereby enhancing the precipitation over the downwind areas (Baik et al., 2001; Han and Baik, 2008). The increased surface roughness over urban areas reduces wind speeds and enhances convergence and precipitation (Collier, 2006; Shem and Shepherd, 2009; Thielen et al., 2000). Additionally, the urban structures cause convective systems to split on both sides of the city and rejoin on the leeward side, affecting the rainfall distribution (Niyogi et al., 2011; Yu et al., 2017; Zhang et al., 2017). Urban aerosols also influence precipitation through effects on radiation and cloud nucleation (Borys et al., 2003; Ntelekos et al., 2009; Rosenfeld, 2000; Waliser and Guan, 2017). However, the impacts of urbanization on precipitation may vary across cities or storm cases (Liu and Niyogi, 2019; Ma et al., 2024), and the conclusions can be different even for the same case because various mechanisms might operate simultaneously (Ma et al., 2024; Qian et al., 2022; Shen and Yang, 2023; Yang et al., 2021). Regarding the "21·7" Henan extremely heavy rainfall event during 17–22 July 2021, Huang et al. (2022) found that the thermal disturbances and increased surface roughness in urban areas promoted water vapor convergence and vertical uplift, resulting in intensified rainfall in the urban areas of Zhengzhou. However, Luo et al. (2023) emphasized that the heating effects and enhanced drying effects in the upstream urban area reduced the water vapor transported to Zhengzhou, thereby reducing rainfall there.

Previous studies have emphasized the significant role of terrain and urban surfaces in EP events (Gao et al., 2022b; Huang et al., 2022; Li et al., 2023; Luo et al., 2023; Wei et al., 2023). However, for the "21·7" EP event, the impact of the underlying surface effects remains highly uncertain, limiting the ability to accurately forecast such events (Luo et al., 2023; Yao and Li, 2023). Most existing research primarily focuses on individual cases, exploring the influence of topography and urban surfaces on EP. However, case studies come with uncertainties and randomness, lacking generalizability. Few studies have systematically analyzed the general role of terrain and urban surfaces in similar catastrophic EP events. Additionally, existing research indicates that large-scale circulation patterns cannot fully explain EP events (Xu et al., 2022; Zhang et al., 2023). Terrain and urban surfaces may significantly impact the EP under similar synoptic patterns (Zhang et al., 2022), but these studies have not quantified their specific roles. There is also a lack of quantitative research on the dynamic and thermodynamic mechanisms by which terrain and urban surfaces influence EP under similar synoptic patterns.

In this study, we first employ spectral clustering techniques to identify the typical synoptic patterns of regional hourly extreme precipitation events (RHEPE) in Henan. Then, through numerical sensitivity experiments, we quantify the impacts and mechanisms of terrain and urban surfaces on RHEPE. Here, we aim to address three special questions: 1) Are there RHEPEs with synoptic patterns similar to the "21·7" EP event in Henan and nearby areas historically? 2) What are their common characteristics? 3) What are the general impacts and physical mechanisms of terrain and urban surfaces on RHEPEs from the perspective of dynamic and thermodynamic processes under a similar synoptic pattern?

2. Data, Method and experiments Design

2.1. Data

The data used in this study are listed as follows:

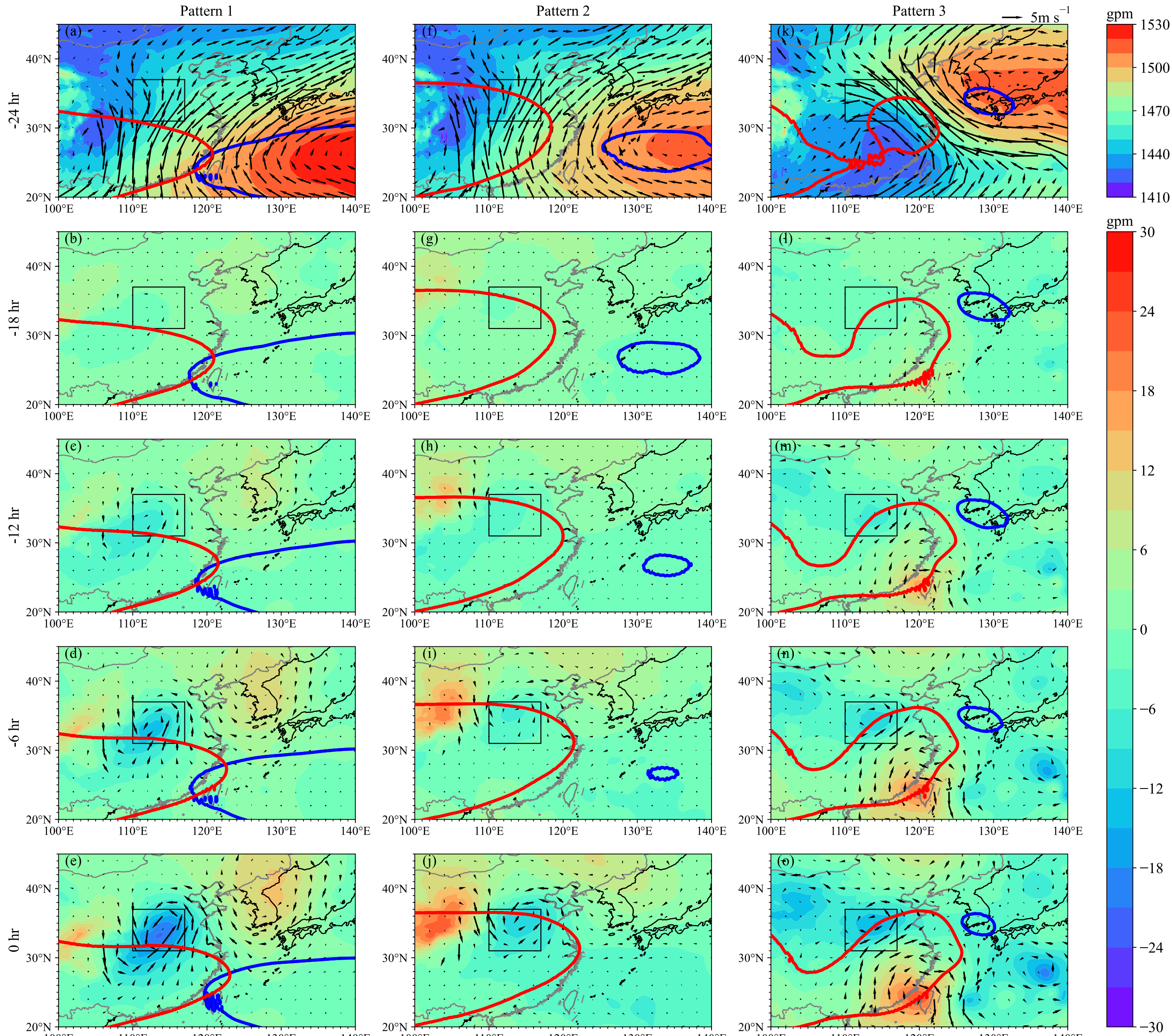

Fig. 3. The composite mean 850 hPa geopotential height (shading) and horizontal wind field (vectors) at 24 h before the RHEPEs (i.e., −24 h) (a, f, and k) and their changes at 18 h (b, g, and l), 12 h (c, h, and m), 6 h (d, i, and n), 0 h (e, j, and o) before the RHEPEs relative to that at 24 h before the RHEPEs under synoptic pattern 1 (1st column), 2 (2nd column) and 3 (3rd column), respectively. The red and blue lines show the SAH at 200 hPa (indicated by the 12,500 gpm contour) and WNPSH at 500 hPa (indicated by the 5880 gpm contour), respectively. The black box denotes the study area. (For interpretation of the references to colour in this figure legend, the reader is referred to the web version of this article.)

1. The hourly gauge observational precipitation data from 229 stations across Henan and surrounding areas during the summertime (June–July-August) from 1980 to 2021 provided by the China Meteorological Administration (CMA), are utilized used to detect the RHEPEs in Henan and nearby areas and validate the precipitation simulated by a regional climate model.
2. The fifth European Centre for Medium-Range Weather Forecasts (ECMWF) reanalysis data (ERA5) (Hersbach et al., 2020), including the geopotential height, zonal and meridional winds, specific humidity, and air temperature with a temporal resolution of 1 h and a horizontal resolution of 0.25° at different vertical layers during 1980–2021 (https://cds.climate.copernicus.eu/cdsapp#!/dataset/reanalysis-era5-pressure-levels?tab=overview), provide the atmospheric initial and lateral boundary conditions, as well as sea surface temperature forcing data of the Weather Research and Forecasting (WRF-ARW) model. The ERA5 reanalysis data are also used for atmospheric circulation classification and model validation.
3. The ERA5-LAND reanalysis dataset (Muñoz-Sabater et al., 2021) provides hourly precipitation data from 1980 to 2021, with a horizontal resolution of 0.1°(https://cds.climate.copernicus.eu/datasets/reanalysis-era5-land?tab=overview).
4. The half-hourly precipitation data from the Integrated Multi-satellite Global Precipitation Measurement (GPM-IMERG V07) from 1998 to 2021, with a horizontal resolution of 0.1° (Huffman et al., 2023), are available at https://disc.gsfc.nasa.gov/datasets/GPM_3IMERGHH_07/summary.
5. The half-hourly precipitation data from the Climate Prediction Center Morphing technique (CMORPH) high-resolution global satellite precipitation estimates from 1998 to 2021, with a horizontal resolution of 8 km (Xie et al., 2019), are available at https://www.

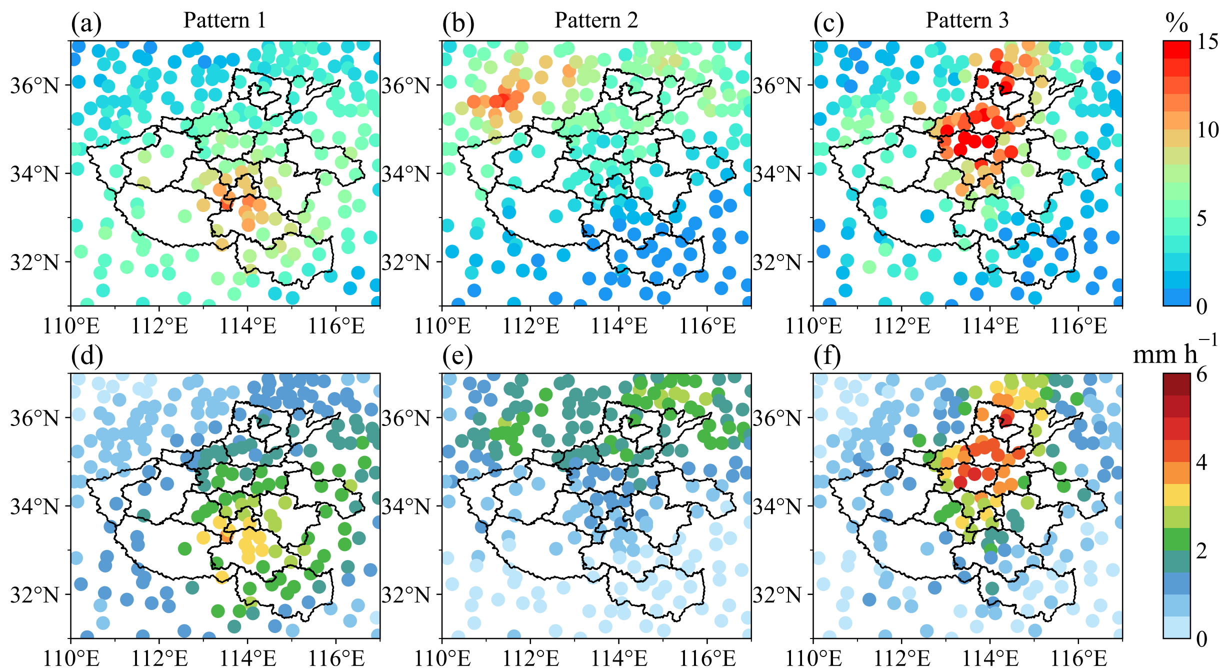

Fig. 4. The spatial distribution of the occurrence probability (a-c) and mean intensity (d-f) of EP at each station under different synoptic patterns of RHEPEs over Henan and surrounding areas during the 42 summers of 1980–2021.

Table 1
SAL values for the WRF-simulated RHEPEs under synoptic pattern 3 within the study area (31–37°N, 110–117°E) from 1998 to 2021 against different observations.

Sources	S	A	L
STATION	0.035	−0.589	0.120
ERA5-LAND	−0.193	−0.049	0.019
GPM	−0.267	−1.015	0.139
CMORPH	−0.010	−1.044	0.165

ncei.noaa.gov/data/cmorph-high-resolution-global-precipitation-estimates/access/30min/8km/.

6. The IGBP modified MODIS land-use categories with a resolution of 30 arc *sec* (Friedl et al., 2010), which is available at https://lpdaac.usgs.gov/products/mcd12q1v006/, is used for land use and terrain representation.

2.2. Definition of RHEPE

Following Tang et al. (2021), an RHEPE, i.e., a high-intensity rainfall event occurring simultaneously across a broad region, is identified through a systematic multi-step process. The process begins by determining an EP threshold for each station within Henan and surrounding areas (Fig. S1a). This is achieved by ranking all instances of hourly precipitation with an intensity $\geq$0.1 mm h^{-1} during the summer seasons from 1980 to 2021 in ascending order. The 95th percentile value of this ranked series is then established as the EP threshold at each station. Next, the 95th percentile of the number of stations experiencing simultaneous EP across the study area during the same period is calculated to define the regional threshold for RHEPE detection. Finally, an RHEPE is identified at a given time if the number of stations experiencing EP events simultaneously exceeds the regional threshold. Using this approach, we detected 2010 RHEPEs across the 42 summers from 1980 to 2021.

2.3. Clustering method

The dominant synoptic patterns leading to the RHEPE occurrences over Henan and nearby areas are categorized using the spectral clustering method, which outperforms the conventional K-means clustering by demonstrating enhanced adaptability to diverse data distributions and greater efficacy in clustering sparse datasets (Ningombam et al., 2024; von Luxburg, 2007). Initially, we select the u and v wind components at 925, 850, 700, 500, and 200 hPa over Henan and surrounding areas (Fig. S1a) during each RHEPE. Subsequently, during a given RHEPE, the u and v wind field arrays (dimensions: levels: 5, latitude: 25, longitude: 29) are converted into one-dimensional arrays (5 × 25 × 29 = 3625 elements). The v array is appended to the u array, creating a comprehensive spatial array containing 7250 elements. A two-dimensional array (2010 × 7250) of 2010 RHEPEs constitutes the input matrix. The clustering results are determined by internal clustering indices (i.e., the Calinski-Harabasz index, Silhouette index, and Davies-Bouldin index), resulting in three clusters (figure now shown).

2.4. Moisture budget analysis

The moisture budget analysis is conducted based on the below equation (Akinsanola and Zhou, 2019; Li et al., 2018; Seager et al., 2010; Zhao et al., 2020a):

$$P = -\frac{1}{g}\int_{P_s}^{P_t}\frac{\partial q}{\partial t}dp - \frac{1}{g}\int_{P_s}^{P_t}\left(\overrightarrow{V_h}\bullet\nabla_h q\right)dp - \frac{1}{g}\int_{P_s}^{P_t}\left(q\nabla_h\bullet\overrightarrow{V_h}\right)dp + E + res, \quad (1)$$

where P denotes the rate of precipitation (mm h^{-1}) and $-\frac{1}{g}\int_{P_s}^{P_t}\frac{\partial q}{\partial t}dp$ indicates the local temporal variation in moisture. $-\frac{1}{g}\int_{P_s}^{P_t}\left(\overrightarrow{V_h}\bullet\nabla_h q\right)dp$and $\frac{1}{g}\int_{P_s}^{P_t}\left(q\nabla_h\bullet\overrightarrow{V_h}\right)dp$ represent the moisture convergence contributed by the horizontal moisture advection and horizontal wind convergence, respectively. E is the evaporation rate and res is the residual term. The g, q, and $\overrightarrow{V_h}$ are the acceleration of gravity (m s^{-2}), specific humidity (kg kg^{-1}), and horizontal wind vector (m s^{-1}), respectively. P_s is the surface pressure (Pa), and P_t is the pressure at the

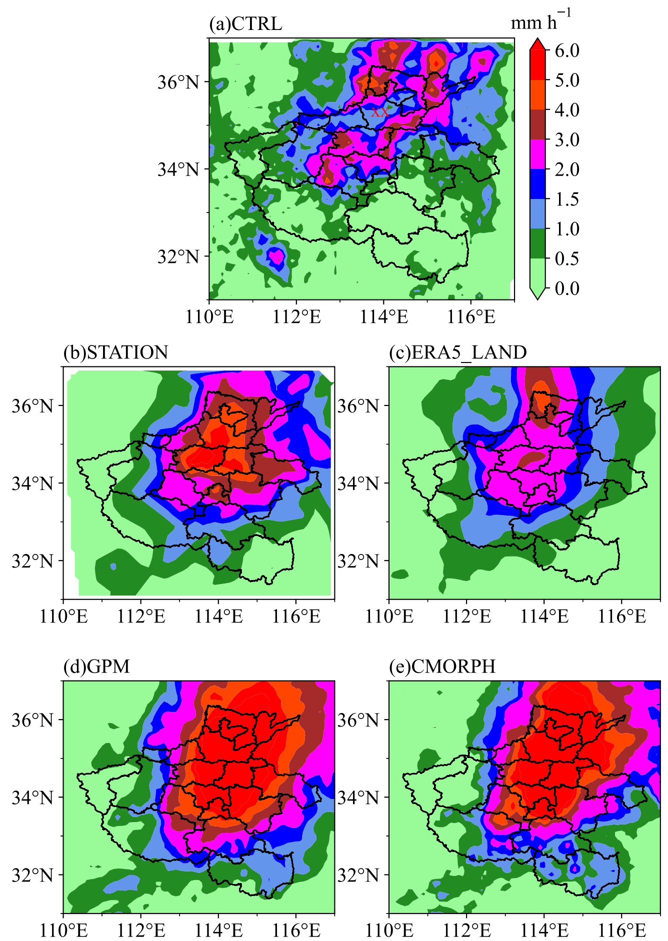

Fig. 5. Spatial distribution of mean precipitation from WRF simulations (a), rain gauge station (b), ERA5-LAND (c), GPM (d), and CMORPH (e) during RHEPEs from 1998 to 2021 under synoptic pattern 3. XX in (a) indicates the Xinxiang area.

top of the troposphere (Pa). Based on the mass conservation equation, it can be inferred that $\left\langle q\nabla_h \bullet \overrightarrow{V_h} \right\rangle = -\langle q\partial_p\omega \rangle$, where "" represents the vertical mass integration throughout the entire troposphere (Chou et al., 2013). Assuming that ω is zero both at the surface and the tropopause (i.e., $\langle \partial_p\omega q \rangle = 0$), we can obtain $-\left\langle q\nabla_h \bullet \overrightarrow{V_h} \right\rangle = -\langle \omega\partial_p q \rangle$. Consequently, the vertical moisture advection corresponds to the horizontal wind convergence term (Seager et al., 2010). The primary contribution to vertical moisture advection comes from lower tropospheric convergence, which facilitates the upward transport of moisture, ultimately resulting in precipitation formation (Akinsanola and Zhou, 2019; Li et al., 2018).

The changes in the moisture budget equation due to the terrain or urban impact are expressed as follows:

$$\Delta P = -\frac{1}{g}\int_{P_s}^{P_t} \Delta\frac{\partial q}{\partial t}dp - \frac{1}{g}\int_{P_s}^{P_t} \Delta\left(\overrightarrow{V_h} \bullet \nabla_h q\right)dp - \frac{1}{g}\int_{P_s}^{P_t} \Delta\left(q\nabla_h \bullet \overrightarrow{V_h}\right)dp + \Delta E + \Delta res, \quad (2)$$

which can be calculated as the difference between control experiments and sensitivity experiments. The changes in horizontal moisture advection and horizontal wind convergence can be further decomposed as follows (Seager et al., 2010; Yuan et al., 2021):

$$-\frac{1}{g}\int_{P_s}^{P_t} \Delta\left(\overrightarrow{V_h} \bullet \nabla_h q\right)dp = -\frac{1}{g}\int_{P_s}^{P_t} \overline{\overrightarrow{V_h}} \bullet \nabla_h(\Delta q)dp - \frac{1}{g}\int_{P_s}^{P_t} \Delta\overrightarrow{V_h} \bullet \nabla_h \overline{q}dp, \quad (3)$$

$$-\frac{1}{g}\int_{P_s}^{P_t} \Delta\left(q\nabla_h \bullet \overrightarrow{V_h}\right)dp = -\frac{1}{g}\int_{P_s}^{P_t} \Delta q\nabla_h \bullet \overline{\overrightarrow{V_h}}dp - \frac{1}{g}\int_{P_s}^{P_t} \overline{q}\nabla_h \bullet \Delta\overrightarrow{V_h}dp, \quad (4)$$

where overbars represent the means of control and sensitivity experiments. $-\frac{1}{g}\int_{P_s}^{P_t} \overline{\overrightarrow{V_h}} \bullet \nabla_h(\Delta q)dp$and $-\frac{1}{g}\int_{P_s}^{P_t} \Delta q\nabla_h \bullet \overline{\overrightarrow{V_h}}dp$represent

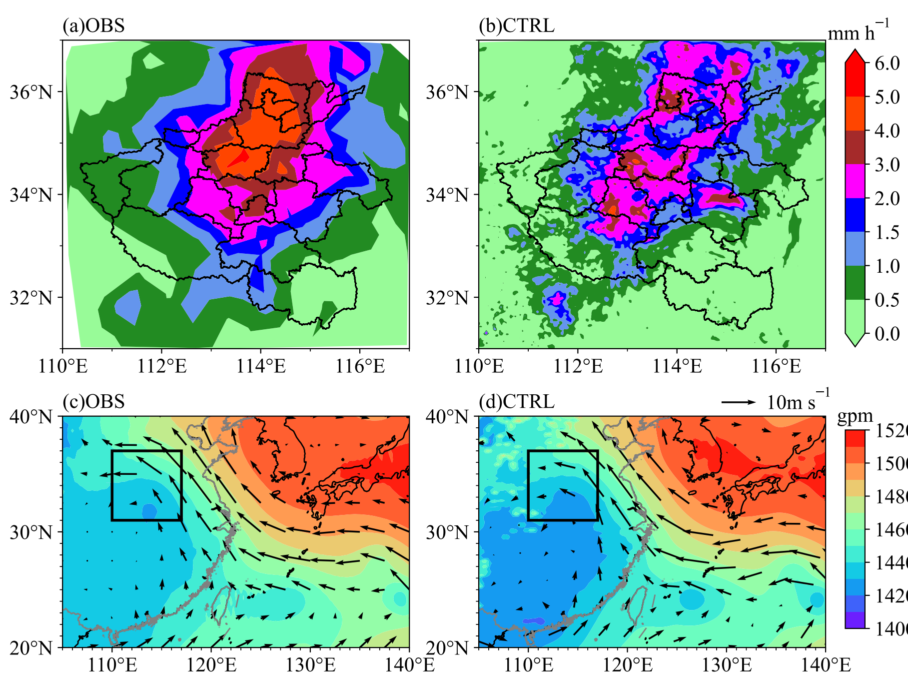

Fig. 6. The spatial distribution of mean precipitation (a,b) and geopotential height (shading) and wind field (vectors) at 850 hPa (c, d) from observation (a, c) and CTRL simulation (b, d) during the 21 cases of RHEPEs (see details in section 2.6) under synoptic pattern 3. The black box denotes the study area.

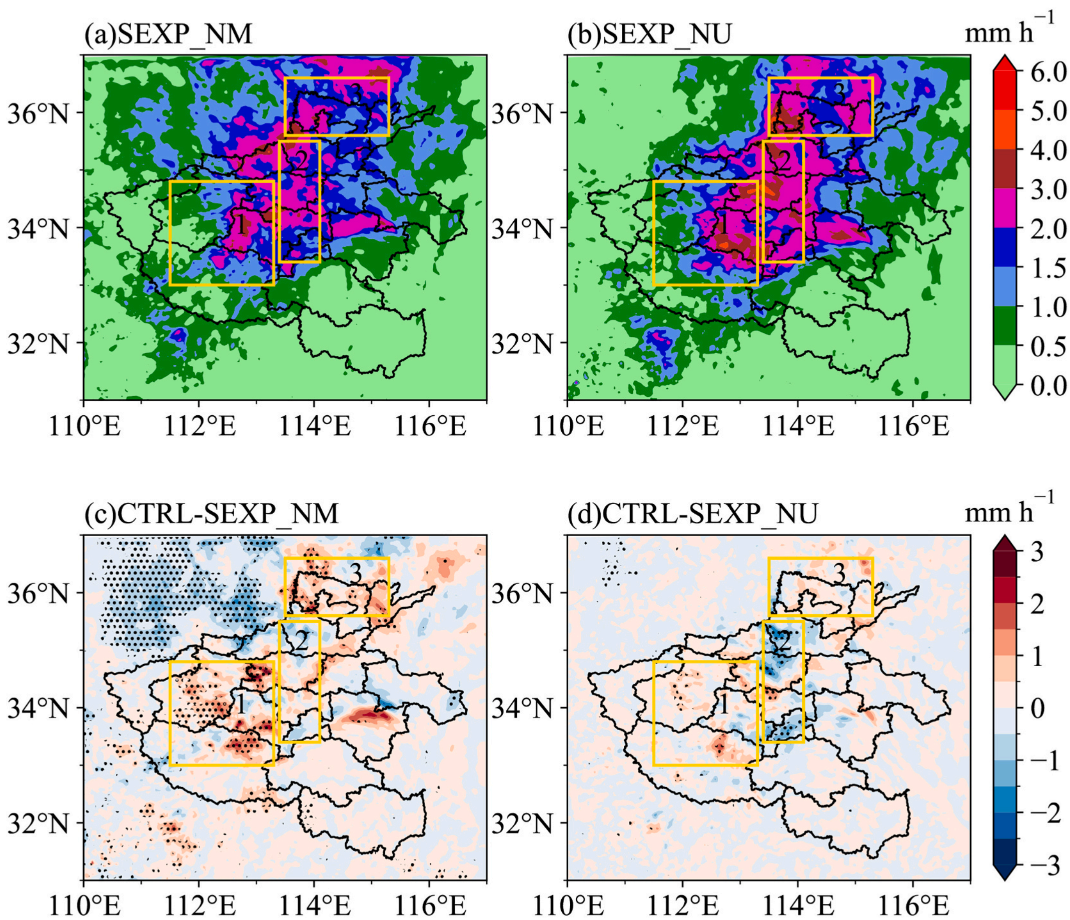

Fig. 7. The spatial distribution of the mean precipitation (a and b) simulated by the SEXP_NM (a) and SEXP_NU (b) experiments and their differences (c and d) from the CTRL experiments during the 21 cases of RHEPEs. Dots in (c) and (d) indicate the differences are statistically significant at a confidence level of 0.05 (*t*-test). The yellow boxes represent three sub-regions: reg1, reg2, and reg3, respectively. (For interpretation of the references to colour in this figure legend, the reader is referred to the web version of this article.)

Table 2
The intensity and occurrence probability of EP under synoptic pattern 3 regionally averaged over the Reg1, Reg2, Reg3, and the whole study region. The bilinear interpolation method was used to interpolate the simulation experiment results to the observation stations and compare them with the station's extreme precipitation thresholds.

	intensity (mm h^{-1})				occurrence probability (%)			
Experiment	Reg1	Reg2	Reg3	Henan	Reg1	Reg2	Reg3	Henan
CTRL	1.81	2.04	2.41	1.30	6.18	5.89	6.98	4.67
SEXP_NM	1.35	2.02	1.91	1.14	4.22	6.20	5.65	4.01
SEXP_NU	1.65	2.51	2.28	1.31	5.64	8.20	6.34	4.85

the thermodynamic terms (i.e., the contributions of water vapor change) in horizontal moisture advection (THA) and horizontal wind convergence (THC), respectively. $-\frac{1}{g}\int_{P_s}^{P_t}\Delta\overrightarrow{V_h}\bullet\nabla_h\overline{q}dp$and $-\frac{1}{g}\int_{P_s}^{P_t}\overline{q}\nabla_h\bullet\Delta\overrightarrow{V_h}dp$ stand for the dynamic terms (i.e., the contributions of circulation change) in horizontal moisture advection (DYA) and horizontal wind convergence (DYC), respectively.

2.5. Model Configuration

This study employs the advanced research version 4.1 of the WRF-ARW model (Skamarock et al., 2019) to investigate the impacts of urban surfaces and terrain on the RHEPEs in Henan and surrounding areas. Three one-way nested domains are configured with a grid spacing of 27 km, 9 km, and 3 km, with the innermost domain covering Henan Province (Fig. S1b). There are 38 sigma levels from the surface to 50 hPa. The atmospheric initial and lateral boundary conditions are derived from the ERA5 hourly data.

The key physical parameterization schemes adopted in the current study are listed as follows: the Lin microphysical scheme (Chen and Sun, 2002), the Rapid Radiative Transfer Model for Universal (RRTMG) longwave and shortwave radiation scheme (Iacono et al., 2008), Mellor-Yamada-Nakanishi and Niino (MYNN) level 2.5 closure planetary boundary layer scheme (Olson et al., 2019), MYNN surface layer scheme (Nakanishi and Niino, 2006), Noah land surface scheme (Tewari et al., 2004). The Kain-Fritsch cumulus convection scheme (Kain, 2004) is turned on in the outer two domains (Fig. S1b) but deactivated in the innermost domain. The Single-Layer Urban Canopy Model (Chen et al., 2011) is used to improve the simulations of surface properties and land-atmospheric interactions over urban areas.

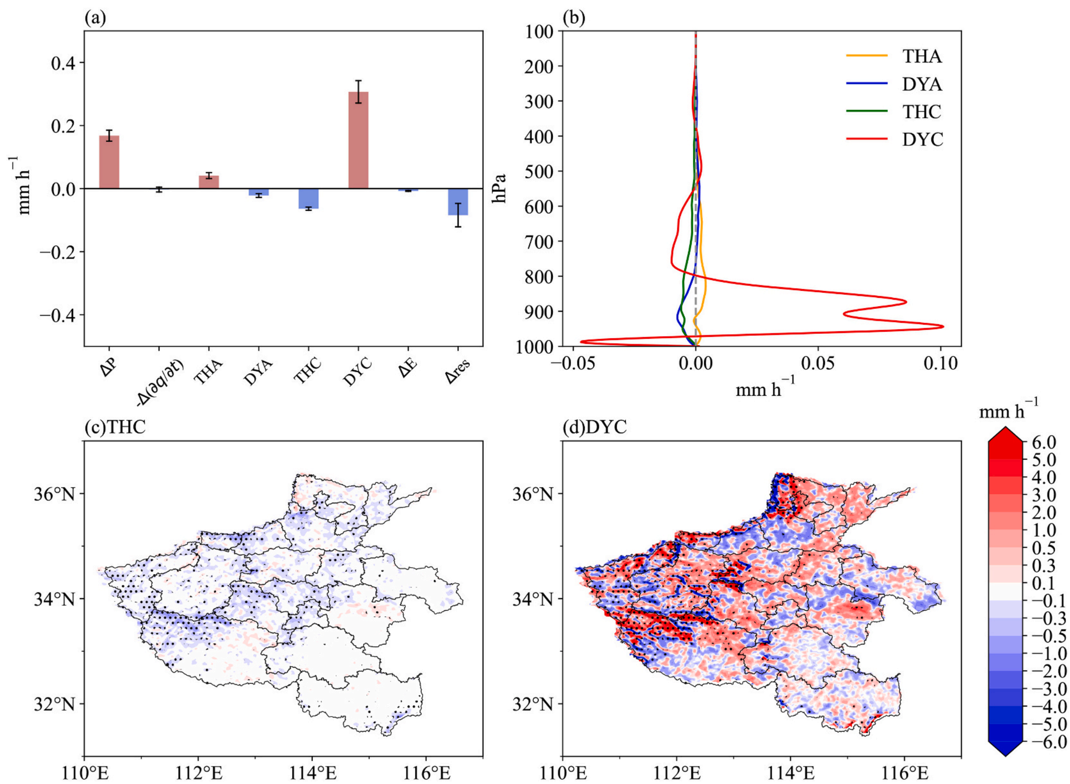

Fig. 8. The mean terrain-induced differences (i.e., CNTL minus SEXP_NM) in various moisture budget components (see Eq. 2–4) regionally averaged over Henan during the 21 cases of RHEPEs (a). The whiskers represent the standard error of each term across different simulation cases. Vertical profiles of the mean terrain-induced differences in THA, DYA, THC, and DYC (b). The spatial distributions of the terrain-induced differences in THC (c) and DYC (d), and the dots in (c) and (d) indicate the differences are statistically significant at a confidence level of 0.05 (t-test).

2.6. Numerical experimental design

Numerical experiments are performed to reveal how the urban surfaces and terrain affect the RHEPEs under synoptic pattern which leads to the most extreme RHEPE (see the explanation in Section 3.1). Under this synoptic pattern, if any RHEPE occurs within 12 h before or after another RHEPE, they are merged into a single case. To save computational resources, cases containing less than two RHEPEs within 24 h are excluded. This process yields 21 cases containing 259 RHEPE hours, which account for 91.5 % of RHEPEs under the synoptic pattern mentioned above.

For each of the 21 cases, we design three experiments with different terrain or urban surface configurations. The CTRL experiment adopts the default terrain (Fig. 1a) and urban surface settings (Fig. 1d). In the SEXP_NM experiment, the altitudes of the western and northern Henan and surrounding mountains above 500 m are set to the mean altitude of the eastern Henan plain (i.e., 59.9 m) (Figs. 1b and e). In the SEXP_NU experiment, the urban land cover type is changed to the cropland near the urban areas (Figs. 1c and f). In each of the 21 RHEPE cases mentioned above, each experiment starts 12 h before the occurrence of the first RHEPE hour and ends 12 h after the last RHEPE hour. The results within the first 12 h are discarded as model spin-up time.

3. Results

3.1. Dominant synoptic patterns of the RHEPEs

The classification of atmospheric circulation shows that the typical synoptic patterns leading to the RHEPEs over Henan and surrounding areas can be divided into three categories (Fig. 2). In synoptic pattern 1, there is a closed contour of 1430 gpm at 850 hPa in southwestern Henan (Fig. 2a), suggesting a strong low-level vortex. In the synoptic pattern 2, there also exists a low-level vortex indicated by a closed contour of 1440 gpm dominating the northwestern part of Henan at 850 hPa (Fig. 2b). Synoptic patterns 1 and 2 account for 85.9 % of the total RHEPE occurrences. Both patterns are accompanied by a trough at 500 hPa (Figs. 2d and e), but they differ in locations and intensities. Synoptic pattern 3, which leads to 14.1 % of the total RHEPE occurrences, is characterized by double tropical cyclones located around 140°E and 125°E in the western Pacific (Fig. 2c) with the northwestward shift of Western North Pacific Subtropical High (WNPSH) (Fig. 2f). The strong southeasterly winds bring abundant moisture to the Henan and surrounding areas (Figs. 2c and f).

Figs. 3a-e show that an anomalous cyclone at 850 hPa develops over southern Henan and continues to move northeastward and intensify during the 24 h to 0 h before RHEPE under synoptic pattern 1. By contrast, the intensities and locations of South Asian high (SAH) at 200 hPa (Figs. 3a-e) and the WNPSH at 500 hPa (Figs. 3a-e) are relatively stable. Under synoptic pattern 2 (Figs. 3f-j), an anomalous cyclone appears over northern Henan at about 6 h before the RHEPE, suggesting that the time required to develop RHEPE is much shorter than the synoptic pattern 1. Compared with the synoptic pattern 1, the SAH is situated further north and almost covers the entire Henan under synoptic pattern 2 (Figs. 3f-j), meanwhile, the area of WNPSH at 500 hPa continues to shrink during the 24 h to 0 h before RHEPE under synoptic pattern 2. Under synoptic pattern 3, a landfalling tropical cyclone on the southeastern coast of China appears 24 h before the RHEPE (Fig. 3k). During 18 h to 0 h before the RHEPE, an anomalous cyclone starts to develop and intensify in Henan, accompanied by an intensified anomalous anticyclone in the southeastern coastal region, corresponding to the inland movement of the tropical cyclone (Figs. 3k-o).

Figure 4 shows the spatial distribution of the occurrence probability and intensity of EP at each station during the RHEPEs under each synoptic pattern. From Figs. 4b, c, e, and f, the stations with a much higher

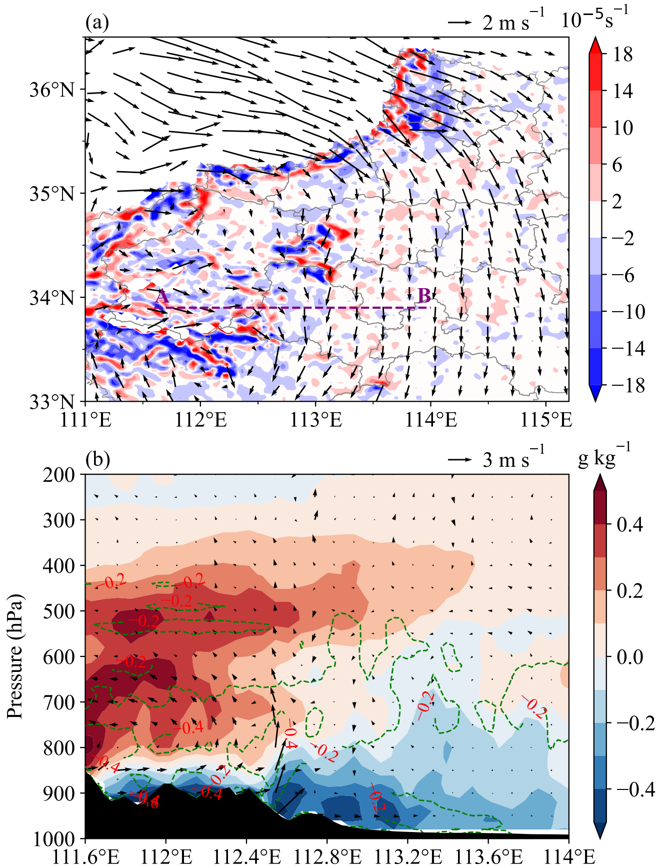

Fig. 9. The spatial distribution of the mean terrain-induced difference in wind field (vectors) and divergence (shading) at 850 hPa (a) during the 21 cases of RHEPEs. Vertical cross-section of the terrain-induced differences (b) in the specific humidity (shading), temperature (green dotted line, K), and the horizontal and vertical winds (vectors; the vertical velocity is enlarged by 10 times) along the A-B purple line in (a). The black shadings in (b) represent topography. (For interpretation of the references to colour in this figure legend, the reader is referred to the web version of this article.)

occurrence probability of EP are located on the western (eastern) side of the Taihang mountains under synoptic pattern 2 (3), indicating that the terrain and land surfaces play an important role in the RHEPE. Under synoptic pattern 3, the stations with the occurrence probability (intensity) of EP exceeding 10 % (3 mm h^{-1}) contribute to 14.8 % (15.3 %) of the total stations within the study area (Figs. 4c and f) and are significantly higher than those under the other synoptic patterns of RHEPEs.

Meanwhile, synoptic pattern 3 encompasses all 50 RHEPEs of the "21·7" EP event, which is the most extreme rainfall event in Henan over the past 40 years and causes huge losses. The synoptic pattern 3 is the most extreme pattern and is also similar to the "21·7" EP event. Therefore, in the following sections, we will conduct numerical sensitivity experiments on multiple cases to focus on how the terrain and urban surface affect the RHEPE under synoptic pattern 3. This may help to better understand the physical processes and possible mechanisms leading to the formation of RHEPEs similar to the "21·7" EP event.

3.2. The effects of terrain and urban surfaces on the RHEPEs under synoptic pattern 3

3.2.1. Model validation

To objectively evaluate the rainfall simulated by the WRF model, we employed the Structure, Amplitude, Location (SAL) method (Wernli et al., 2008) for quantitative precipitation verification. Meanwhile, we integrated multi-source precipitation observation data, including rain gauge stations, ERA5-LAND, GPM, and CMORPH data. Since GPM and CMORPH data have only been available since 1998, the precipitation data in the following analysis are limited to the RHEPEs in synoptic pattern 3 between 1998 and 2021. For the convenience of subsequent comparative calculations, we performed bilinear interpolation on both the WRF simulation data and all observation data, with a resolution of 0.1° × 0.1°. The results of the quantitative evaluation are presented in Table 1. The model exhibits a large error in the amplitude (A) component, particularly when compared against GPM and CMORPH (i.e., A < -1), suggesting that the magnitude of precipitation is largely underestimated. By contrast, the structural (S) and location (L) components are relatively small, indicating that the WRF model well simulates the spatial pattern of precipitation The spatial distributions of precipitation are given in Fig. 5, which shows that WRF successfully captures the strong precipitation center in the central and northern parts of Henan. The main error stems from the failure to capture the precipitation center near Xinxiang.

Due to the absence of the GPM and CMORPH data between 1980 and 1997, only the rain gauge station observations are used to validate the simulated RHEPEs from 1980 to 2021. As shown in Fig. 6a and b, the CTRL experiment successfully reproduced the spatial distribution of the observed rainfall, although the intensity of the rainfall center was slightly underestimated. The spatial correlation coefficient between the CTRL rainfall simulation and the observations is 0.83, which is significant at the 99 % confidence level. Meanwhile, the 850 hPa atmospheric circulation field simulated by the CTRL experiment is generally

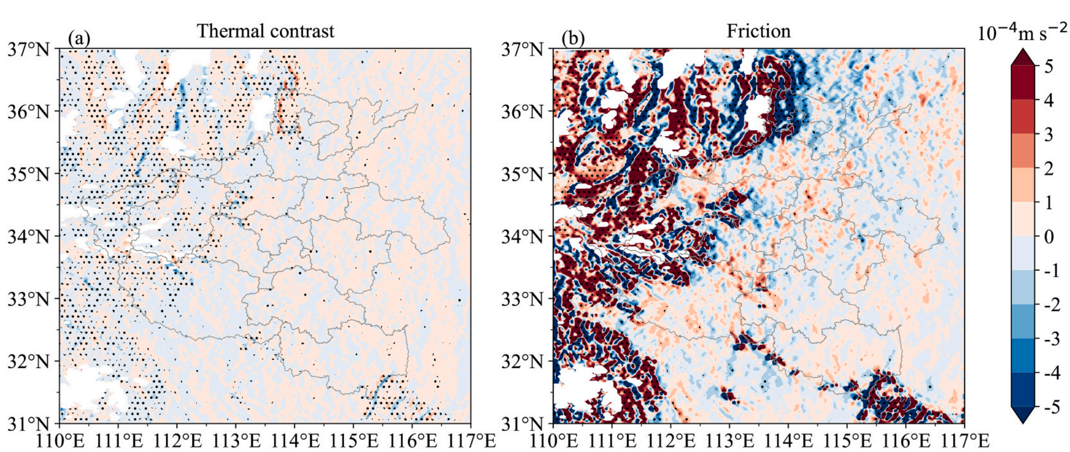

Fig. 10. Spatial distributions of the mean terrain-induced differences (i.e., CNTL minus SEXP_NM) in thermal contrast term (a) and friction term (b) calculated according to Eq. 5. The dots indicate that the results passed the significance test at the 0.05 level.

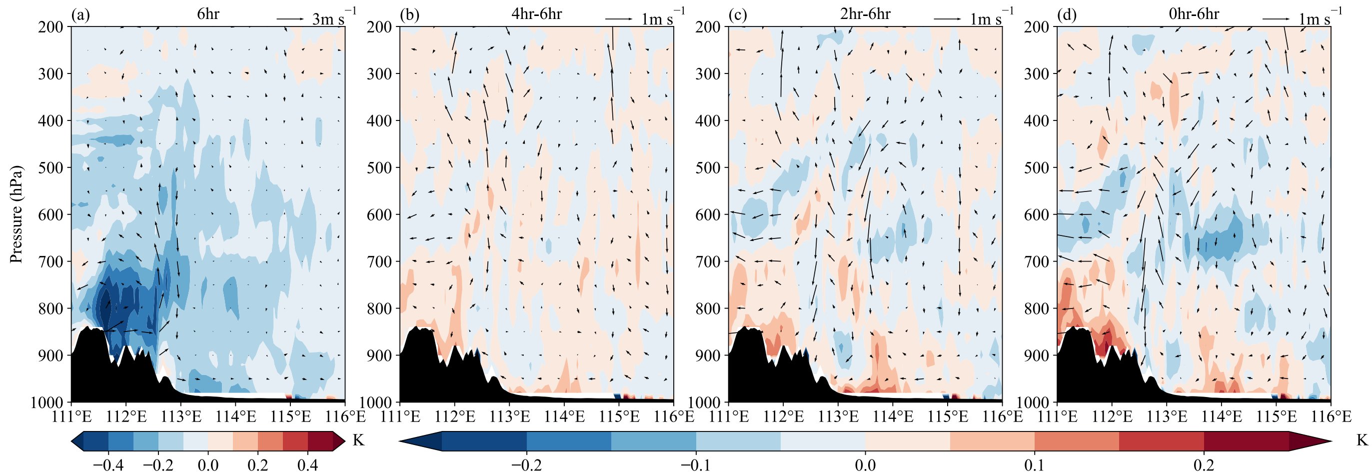

Fig. 11. Terrain-induced differences (i.e., CNTL minus SEXP_NM) in temperature (shaded, K) and wind vector distributions (vertical wind multiplied by 10) 6 h before the RHEPE (a), along with the temperature differences (shaded, K) and wind vector differences (vertical wind multiplied by 10) at 4 h (b), 2 h (c), and 0 h (d) before the RHEPE relative to 6 h prior in the CTRL experiments, shown along the purple line A-B in Fig. 9a. (For interpretation of the references to colour in this figure legend, the reader is referred to the web version of this article.)

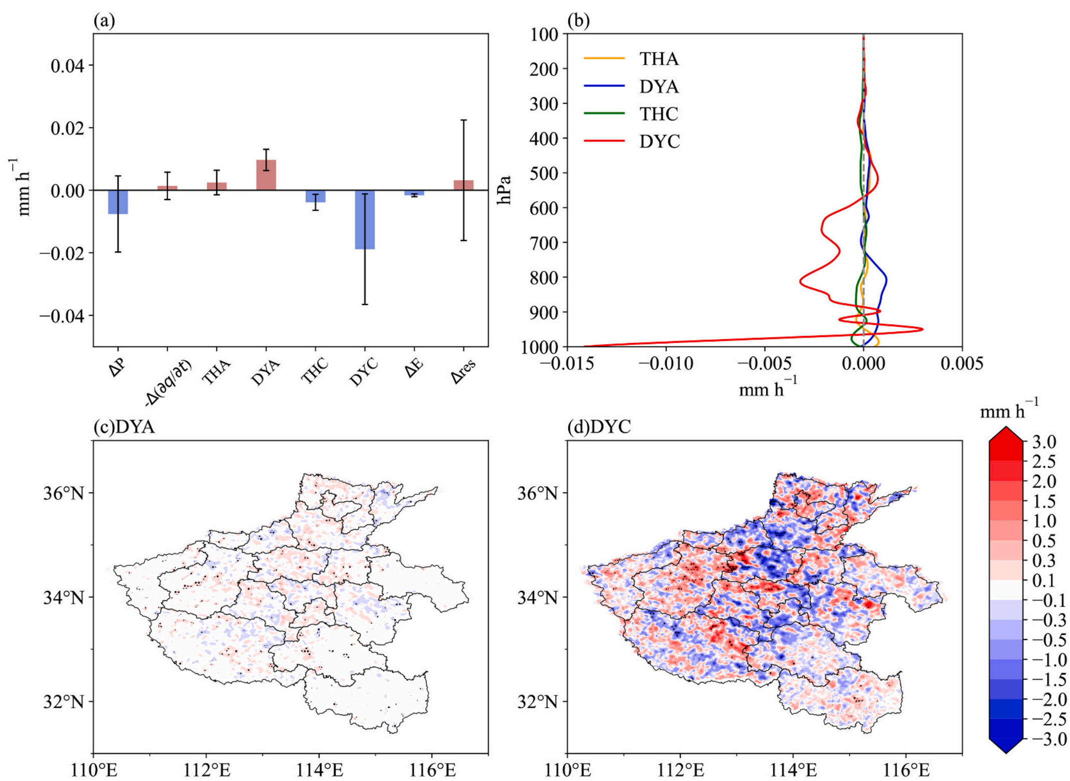

Fig. 12. Same as Fig. 8a, b, but for the urban-induced differences (i.e., CTRL minus SEXP_NU) (a and b). The spatial distributions of the urban-induced differences in DYA (c) and DYC (d), with the meaning of dotted areas the same as in Fig. 8c, d.

consistent with the ERA5 data (Fig. 6c and d), indicating that WRF can well simulate the precipitation and large-scale circulation under synoptic pattern 3, and thus is suitable for studying the effects of topography and urban surfaces on RHEPE.

3.2.2. Impacts of terrain and urban surfaces on the RHEPEs

From Figs. 7a-d, the significant impacts of terrain or urban surfaces on the mean intensity and occurrence probability of EP during the RHEPEs under synoptic pattern 3 are located in three subregions: Reg 1 (including the windward slope of Funiu Mountains in western Henan), Reg 2 (major urban areas in central Henan), and Reg 3 (encompassing the windward slope of Taihang Mountains in northern Henan).

From Fig. 7c and Table 2, the existence of terrain can increase the precipitation intensity regionally averaged over the windward slope of the Funiu Mountains (Reg1) by 34.1 % or 0.46 mm h^{-1} and the precipitation regionally averaged over the windward slope of the Taihang Mountains (Reg3) by 26.2 % or 0.5 mm h^{-1}. Meanwhile, the terrain can lead to the occurrence probability of EP increased by 46.4 % and 23.5 % in Reg 1 and Reg 3, respectively (Table 2). Overall, the intensity (occurrence probability) of EP regionally averaged over the Henan Province can be increased by 14.0 % (16.5 %) due to the terrain under synoptic pattern 3 of the RHEPEs over the Henan and nearby areas.

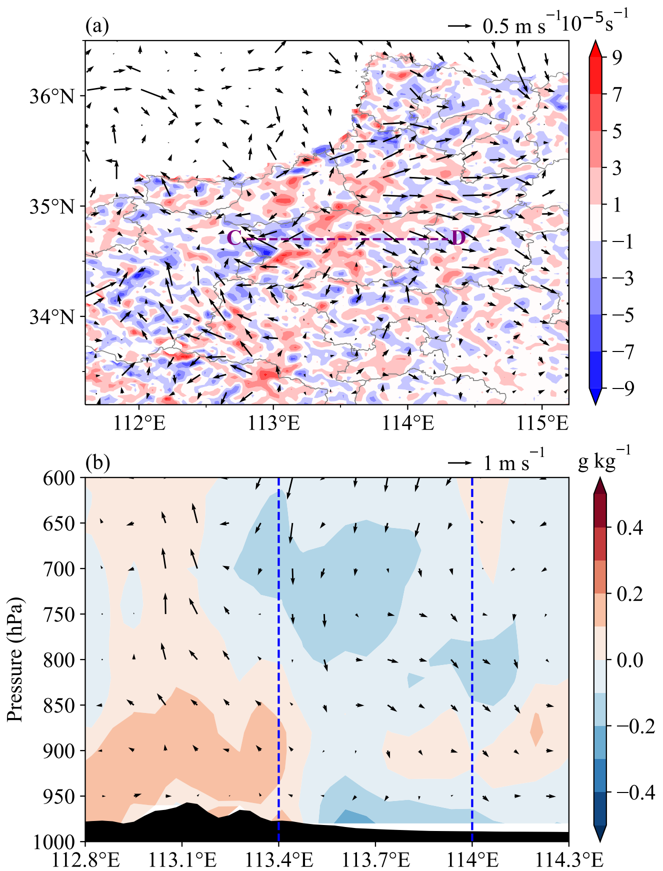

Fig. 13. The spatial distribution of the mean urban-induced difference in wind field (vectors) and divergence (shading) at 850 hPa (a) during the 21 cases of RHEPEs. Vertical cross-section of the mean urban-induced differences (b) in the specific humidity (shading) and the horizontal and vertical winds (vectors; the vertical velocity is enlarged by 10 times) along the C—D purple line in (a). The black shadings in (b) represent topography and the blue dashed lines represent the main urban area of Zhengzhou. (For interpretation of the references to colour in this figure legend, the reader is referred to the web version of this article.)

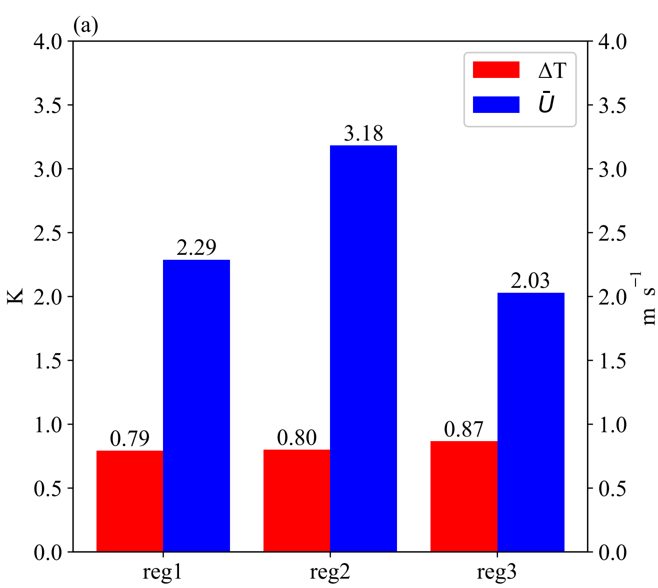

Fig. 14. Average UHI and wind speed in different sub-regions in Fig. 7d in the CTRL experiments.

In contrast to terrain, the impacts of urban surfaces on the intensity and occurrence probability of EP are mainly located in the major urban areas in central Henan (i.e. Reg 2), where the intensity and occurrence probability of EP are significantly reduced by the urban surfaces (Fig. 7d and Table 2). In addition, the urban surfaces slightly enhance precipitation in the downwind region (i.e., Reg 1). The urban surfaces reduce the intensity of EP by 1 % and the occurrence probability of EP by 4 % when regionally averaged over Henan.

3.2.3. Possible physical mechanisms

In this study, we investigate the physical mechanisms associated with the impacts of terrain and urban surfaces on RHEPEs in Henan Province under synoptic pattern 3. Using moisture budget decomposition, we find that terrain-induced changes in precipitation are primarily driven by enhancements in the thermodynamic term of horizontal moisture advection (THA) and the dynamic term of horizontal wind convergence (DYC), whose effects are partially offset by reductions in the dynamic term of horizontal moisture advection (DYA) and the thermodynamic term of horizontal wind convergence (THC) (Fig. 8a). The response of DYC is mainly found in the low-to-middle atmosphere, with relatively larger increases at 1000–800 hPa and relatively small decreases at 800–600 hPa (Fig. 8b). Differently, the THC is reduced throughout the low-to-middle atmosphere (Fig. 8b).

The effects of terrain on THC and DYC are primarily located on the windward slopes of the mountains (Figs. 8c and d). Notably, the spatial pattern of the response in DYC closely matches that of precipitation (Figs. 8c and 7c), indicating the dominant role of DYC in the variation of precipitation in terms of both mean magnitude and spatial distribution.

The increase in the low-level DYC at 1000–850 hPa (Fig. 8b) can be explained by the blocking effects of the Taihang and Funiu Mountains on the horizontal winds (Fig. 9). With the presence of terrain, there are abnormal northerly and westerly winds at 850 hPa, which reduce the strength of prevailing southeasterly and lead to noticeable enhancement in the low-level convergence on the windward slopes in northern and western Henan (Fig. 9a). The atmospheric conditions at different vertical levels are further altered. Taking the cross-section along the Funiu Mountains as an example, the change in the low-level convergence results in enhanced upward motion according to the continuity equation (Fig. 9b), which increases the vertical moisture advection and specific humidity above 800 hPa. Meanwhile, low-level moisture is reduced, which is because of the significant reductions in surface evaporation due to the presence of mountains (figure not shown). Since the background horizontal wind convergence term is positive at 1000–800 hPa and negative at 800–500 hPa (figure not shown), the change in the vertical distribution of moisture induces decreases (increases) in the moisture convergence (divergence) in the low (middle) level, corresponding to the reduction of THC in the entire low-to-middle atmosphere.

The simulation results show that under the background airflow of easterly wind, the terrain mainly increases precipitation by slowing down the low-level wind field on the windward slope and enhancing convergence. Based on momentum balance analysis, this deceleration $\left(\frac{du_0}{dt}\right)$ can be decomposed into contributions from the geopotential gradient force, the Coriolis force, and friction (Gao et al., 2022a; Gao et al., 2024), as follows:

$$\frac{du_0}{dt} = -\frac{\partial\phi}{\partial x} + fv_0 - F_r = -\left.\frac{\partial\phi}{\partial x}\right|_{P_0} - R_d\frac{\partial\langle T_v\rangle}{\partial x}ln\left(\frac{P_0}{P}\right) + R_w + fv_0 - F_r, \quad (5)$$

where ϕ, f, v_0, F_r, R_d, T_v, and R_w represent the geopotential, Coriolis parameter, meridional wind, frictional force, gas constant for dry air, virtual temperature, and residual of non-hydrostatic equilibrium, respectively. Under the conditions of hydrostatic balance, the geopotential gradient force $\left(-\frac{\partial\phi}{\partial x}\right)$ can be further decomposed into the

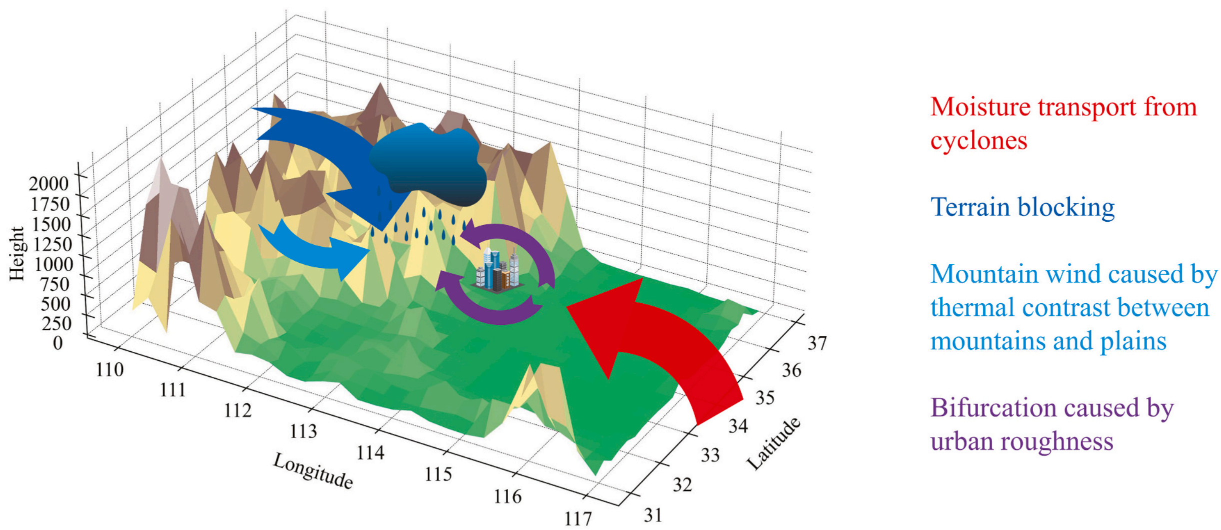

Fig. 15. Schematic diagram of the physical mechanism of the impacts of terrain and urban surfaces on RHEPEs in Henan Province. The colour of the elements in the figure corresponds to the colour of the text.

horizontal gradient force in the free atmosphere $\left(-\frac{\partial\phi}{\partial x}\Big|_{P_0}\right)$, which is related to synoptic systems, and the effects of thermal wind between $P$and $P_0\left(-R_d\frac{\partial\langle T_v\rangle}{\partial x}ln\left(\frac{P_0}{P}\right)\right)$, where $\langle T_v\rangle$ is the average taken between $P$and P_0. The friction term represents the effect of terrain blocking. Therefore, the deceleration of the zonal wind can be attributed to synoptic forcing, thermal contrasts, non-hydrostatic residual, Coriolis, and friction.

Diagnostic analysis indicates that topography causes greater cooling in mountainous areas than in plains (Fig. 9b), and the thermal contrast generates an anomalous westerly wind at lower levels from the mountains to the plains (Fig. 10a), thereby enhancing low-level convergence. However, the impact of thermal contrast on wind field deceleration is much smaller than the effect of topographic blocking (Fig. 10b).

A detailed analysis of the temporal variation in thermal contrast caused by terrain revealed that six hours before the occurrence of the RHEPE, the temperature drop in the mountainous area was much greater than that in the plains, and there was an obvious temperature gradient between the mountains and the plains, resulting in a thermal wind effect (Fig. 11a). However, with the progression of time, the continuous near-surface (near 800hpa) warming over the mountains gradually reduces the thermal contrast between the mountainous and plain areas, thereby weakening its deceleration effect on the background easterly flow (Figs. 11b-d). Consequently, the impact of thermal contrast on wind field deceleration becomes less significant than the blocking effect induced by the terrain.

Figure 12a illustrates the impact of urban surfaces (i.e., CTRL minus SEXP_NM) on moisture budget during the selected RHEPEs regionally averaged over Henan Province, indicating that the influences of dynamic terms (i.e., DYA and DYC) are much greater than that of thermodynamic terms (i.e., THA and THC). The reduction in precipitation is largely due to the decreased DYC. By contrast, DYA is increased, partially offsetting the impact of DYC. The responses of DYC and DYA are mainly seen in the low-to-middle atmosphere between 1000 and 600 hPa (Fig. 12b). The urban-induced reduction in DYC is primarily located in the urban areas of central Henan, while at urban-rural interfaces, especially in the downwind regions of urban, DYC is increased to some degree (Fig. 12d), which is highly consistent with the responses of precipitation caused by the urban surfaces (Fig. 7d).

In central Henan (Fig. 13a), due to the much larger surface roughness compared to the cropland, the urban surfaces result in the anomalous westerly winds at 850 hPa over the urban areas and upwind regions (point D in Fig. 13a). Consequently, the low-level convergence at 850 hPa (contour in Fig. 13a) is reduced over the urban areas, corresponding to the decrease in DYC. Simultaneously, due to the west-to-east gradient of low-level water vapor (figure not shown), anomalous westerlies result in positive anomalies in moisture advection, explaining the increase in DYA (Figs. 12b and c). It is evident that the horizontal winds bifurcate and rejoin in the downwind area (point C in Fig. 13a) when traversing the urban areas, increasing low-level convergence and thereafter DYC in the downwind areas. The vertical cross-section from downwind to upwind areas (Fig. 13b) shows anomalous downward and upward motions in the urban and downwind areas, respectively. This leads to decreased (increased) specific humidity over the urban areas (urban-rural interfaces) via vertical moisture advection.

The UHI effect (ΔT) is defined as the average 2 m air temperature of urban grid points within a 10×10 grid minus the average 2 m air temperature of rural grid points, with the subregional mean calculated by averaging within the subregion. The mean urban canopy wind ($\overline{U}$) is defined as the average 10 m wind speed of all grid points within the subregion. During the RHEPE, the UHI effect slightly increased low-level air temperatures, resulting in a modest enhancement in vertical velocity. However, the increased surface roughness over urban areas led to descending air motion in the urban core. The combined dynamic and thermal effects of urban surfaces resulted in a net decrease in vertical velocity over urban areas, indicating that the dynamic effects associated with urban roughness dominated, while the thermal effects were relatively minor. During the RHEPE, due to relatively high background wind speeds ($\overline{U}$>2 m s^{-1}) and a weak UHI effect (ΔT<0.9 °C), the thermal influence on precipitation was minimized (Fig. 14). This finding is consistent with previous studies (Shen and Yang, 2023; Zhang et al., 2017), which demonstrated that under conditions of strong winds and a weak UHI effect, the thermal contributions of urbanization have limited impacts on precipitation.

4. Summary and discussion

The study identifies three primary synoptic patterns associated with RHEPEs in Henan. The terrain and urban surface impacts on RHEPEs associated with synoptic pattern 3, which is characterized by tropical cyclones and causes the most extreme precipitation events, including the historic “21·7” event, are further investigated based on numerical simulations. The terrain significantly enhances precipitation by increasing wind convergence on the windward slopes, primarily through dynamic blocking effects. Additionally, the deceleration of the wind field induced by the thermal contrast between mountainous and plain areas further promotes convergence, thereby intensifying precipitation (Fig. 15).

The impact of urban surfaces is more localized. Because of the strong wind and weak UHI intensity, the dynamic effects of urban surface play a more substantial role in precipitation compared to its thermal influence. The high roughness of the urban surface leads to the bifurcation of the low-level horizontal wind field. This bifurcation reduces precipitation within central urban areas while enhancing precipitation on both sides of the city and in surrounding suburban areas (Fig. 15).

This study contributes to a better understanding of the relative impacts of terrain and urban surface on regional precipitation patterns under extreme weather conditions, which is important for developing disaster mitigation strategies for areas prone to extreme precipitation. Future research should explore these terrain and urban impacts across various synoptic conditions.

CRediT authorship contribution statement

Shuang Chen: Writing – original draft, Visualization, Validation, Software, Methodology, Investigation, Funding acquisition, Formal analysis, Conceptualization. **Ben Yang:** Writing – review & editing, Supervision, Project administration, Methodology, Investigation, Funding acquisition, Conceptualization. **Anning Huang:** Writing – review & editing, Supervision, Project administration, Methodology, Investigation, Funding acquisition, Conceptualization. **Yan Zhang:** Data curation.

Declaration of competing interest

The authors declare that they have no known competing financial interests or personal relationships that could have appeared to influence the work reported in this paper.

Acknowledgment

This study is supported by the National Natural Science Foundation of China under Grants U2342207 and U2142201, the Open Grants of the State Key Laboratory of Severe Weather (2021LASW-A12) and the Jiangsu Collaborative Innovation Center for Climate Change. We show our deepest appreciation to the High Performance Computing Center of Nanjing University for providing us the computing resources.

Appendix A. Supplementary data

Supplementary data to this article can be found online at https://doi.org/10.1016/j.atmosres.2025.108033.

Data availability

Data will be made available on request.

References

Akinsanola, A.A., Zhou, W., 2019. Dynamic and thermodynamic factors controlling increasing summer monsoon rainfall over the West African Sahel. Clim. Dyn. 52, 4501–4514. https://doi.org/10.1007/s00382-018-4394-x.

Baik, J.-J., Kim, Y.-H., Chun, H.-Y., 2001. Dry and moist convection forced by an urban heat island. J. Appl. Meteorol. 40, 1462–1475. https://doi.org/10.1175/1520-0450(2001)040<1462:Damcfb>2.0.Co;2.

Borys, R.D., Lowenthal, D.H., Cohn, S.A., Brown, W.O.J., 2003. Mountaintop and radar measurements of anthropogenic aerosol effects on snow growth and snowfall rate. Geophys. Res. Lett. 30, 4. https://doi.org/10.1029/2002gl016855.

Changnon, S.A., 1992. Inadvertent weather modification in urban areas: lessons for global climate change. J. Bull. Am. Meteorol. Soc. 73, 619–627. https://doi.org/10.1175/1520-0477(1992)073<0619:IWMIUA>2.0.CO;2.

Chen, F., Kusaka, H., Bornstein, R., Ching, J., Grimmond, C.S.B., Grossman-Clarke, S., Loridan, T., Manning, K.W., Martilli, A., Miao, S., Sailor, D., Salamanca, F.P., Taha, H., Tewari, M., Wang, X., Wyszogrodzki, A.A., Zhang, C., 2011. The integrated WRF/urban modelling system: development, evaluation, and applications to urban environmental problems, 31, 273–288. https://doi.org/10.1002/joc.2158.

Chen, S.-H., Sun, W.-Y., 2002. A one-dimensional time dependent cloud model. J. Meteorol. Soc. Jpn. Ser. II. 80, 99–118. https://doi.org/10.2151/jmsj.80.99.

Chou, C., Chiang, J.C.H., Lan, C.-W., Chung, C.-H., Liao, Y.-C., Lee, C.-J., 2013. Increase in the range between wet and dry season precipitation. Nat. Geosci. 6, 263–267. https://doi.org/10.1038/ngeo1744.

Collier, C.G., 2006. The impact of urban areas on weather. Q. J. R. Meteorol. Soc. 132, 1–25. https://doi.org/10.1256/qj.05.199.

Davis, C.A., Lee, W.C., 2012. Mesoscale analysis of heavy rainfall episodes from SoWMEX/TiMREX. J. Atmos. Sci. 69, 521–537. https://doi.org/10.1175/Jas-D-11-0120.1.

Ding, Y., 2015. On the study of the unprecedented heavy rainfall in Henan Province during 4-8August 1975:Review and assessment. Acta. Meteor. Sin. 73, 411–424.

Fairman Jr., J.G., Nair, U.S., Christopher, S.A., Mölg, T., 2011. Land use change impacts on regional climate over Kilimanjaro. J. Geophys. Res.-Atmos. 116, 24. https://doi.org/10.1029/2010jd014712.

Freitag, B.M., Nair, U.S., Niyogi, D., 2018. Urban Modification of Convection and Rainfall in complex Terrain. Geophys. Res. Lett. 45, 2507–2515. https://doi.org/10.1002/2017gl076834.

Friedl, M.A., Sulla-Menashe, D., Tan, B., Schneider, A., Ramankutty, N., Sibley, A., Huang, X., 2010. MODIS Collection 5 global land cover: algorithm refinements and characterization of new datasets. Remote Sens. Environ. 114, 168–182. https://doi.org/10.1016/j.rse.2009.08.016.

Galewsky, J., Sobel, A., 2005. Moist dynamics and orographic precipitation in northern and Central California during the new year's flood of 1997. Mon. Weather Rev. 133, 1594–1612. https://doi.org/10.1175/mwr2943.1.

Gao, X.Y., Luo, Y.L., Lin, Y.L., Bao, X.H., 2022a. A source of WRF simulation error for the early-summer warm-sector heavy rai-fall over South Cnina Coast: land-Sea thermal Contrast in Boundary Layer. J. Geophys. Res.-Atmos. 127, 25. https://doi.org/10.1029/2021jd035179.

Gao, X.Y., Sun, J.S., Yin, J.F., Abulikemu, A., Wu, C., Liang, X.D., Xia, R.D., 2024. The impact of mountain-plain thermal contrast on precipitation distributions during the "23.7" record-breaking heavy rainfall over North China. Atmos. Res. 310. https://doi.org/10.1016/j.atmosres.2024.107582.

Gao, Z.Q., Zhang, J.B., Yu, M., Liu, Z.Z., Yin, R.Y., Zhou, S.H., Zong, L., Ning, G.C., Xu, X. Z., Guo, Y.Q., Wei, H., Yang, Y.J., 2022b. Role of water vapor modulation from multiple pathways in the occurrence of a record-breaking heavy rainfall event in China in 2021. Earth Space Sci. 9, 14. https://doi.org/10.1029/2022ea002357.

Han, J.-Y., Baik, J.-J., 2008. A theoretical and numerical study of urban heat island-induced circulation and convection. J. Atmos. Sci. 65, 1859–1877. https://doi.org/10.1175/2007jas2326.1.

Hersbach, H., Bell, B., Berrisford, P., Hirahara, S., Horányi, A., Muñoz-Sabater, J., Nicolas, J., Peubey, C., Radu, R., Schepers, D., Simmons, A., Soci, C., Abdalla, S., Abellan, X., Balsamo, G., Bechtold, P., Biavati, G., Bidlot, J., Bonavita, M., De Chiara, G., Dahlgren, P., Dee, D., Diamantakis, M., Dragani, R., Flemming, J., Forbes, R., Fuentes, M., Geer, A., Haimberger, L., Healy, S., Hogan, R.J., Hólm, E., Janisková, M., Keeley, S., Laloyaux, P., Lopez, P., Lupu, C., Radnoti, G., de Rosnay, P., Rozum, I., Vamborg, F., Villaume, S., Thépaut, J.-N., 2020. The ERA5 global reanalysis. Q. J. R. Meteorol. Soc. 146, 1999–2049. https://doi.org/10.1002/qj.3803.

Houze, R.A., 2012. Orographic effects on precipitating clouds. Rev. Geophys. 50, 47. https://doi.org/10.1029/2011rg000365.

Huang, D., Zhu, J., Xiao, X., Cheng, J., Ding, Y., Qian, Y., 2021. Understanding the sensitivity of hourly precipitation extremes to the warming climate over Eastern China. Environ. Res. Commun. 3, 081002. https://doi.org/10.1088/2515-7620/ac17e1.

Huang, X., Wang, D., Li, L.Z.X., Li, Q., Zeng, Z., 2022. Modeling urban impact on Zhengzhou storm on July 20, 2021. J. Geophys. Res.-Atmos. 127, 16. https://doi.org/10.1029/2022jd037387.

Huffman, G.J., Stocker, E.F., Bolvin, D.T., Nelkin, E.J., Tan, J., 2023. GPM IMERG Final Precipitation L3 half Hourly 0.1 degree x 0.1 degree V07. Goddard Earth Sci. Data Inform. Serv. Center (GES DISC) [dataset]. https://doi.org/10.5067/GPM/IMERG/3B-HH/07.

Iacono, M.J., Delamere, J.S., Mlawer, E.J., Shephard, M.W., Clough, S.A., Collins, W.D., 2008. Radiative forcing by long-lived greenhouse gases: calculations with the AER radiative transfer models. J. Geophys. Res.-Atmos. 113, 8. https://doi.org/10.1029/2008jd009944.

Kain, J.S., 2004. The Kain-Fritsch convective parameterization: an update. J. Appl. Meteorol. 43, 170–181. https://doi.org/10.1175/1520-0450(2004)043<0170:Tkcpau>2.0.Co;2.

Li, H., Xi, L., Wang, X.-M., 2023. A high-resolution numerical simulation of the "7.19" extraordinary heavy rainfall in Henan Province under topographic effect. Front. Earth Sci. 10, 13. https://doi.org/10.3389/feart.2022.1079369.

Li, P., Zhou, T., Chen, X., 2018. Water vapor transport for spring persistent rains over southeastern China based on five reanalysis datasets. Clim. Dyn. 51, 4243–4257. https://doi.org/10.1007/s00382-017-3680-3.

Li, X., Zhang, K., Bao, H., Zhang, H., 2022. Climatology and changes in hourly precipitation extremes over China during 1970–2018. Sci. Total Environ. 839, 156297. https://doi.org/10.1016/j.scitotenv.2022.156297.

Liu, H., Huang, X., Fei, J., Zhang, C., Cheng, X., 2022. Spatiotemporal features and associated synoptic patterns of extremely persistent heavy rainfall over China. J. Geophys. Res.-Atmos. 127, 23. https://doi.org/10.1029/2022jd036604.

Liu, J., Niyogi, D., 2019. Meta-analysis of urbanization impact on rainfall modification. Sci. Rep. 9, 14. https://doi.org/10.1038/s41598-019-42494-2.

Luo, Y., Wu, M., Ren, F., Li, J., Wong, W.-K., 2016. Synoptic situations of extreme hourly precipitation over China. J. Clim. 29, 8703–8719. https://doi.org/10.1175/jcli-d-16-0057.1.

Luo, Y., Zhang, J., Yu, M., Liang, X., Xia, R., Gao, Y., Gao, X., Yin, J., 2023. On the Influences of Urbanization on the Extreme Rainfall over Zhengzhou on 20 July 2021: a Convection-Permitting Ensemble Modeling Study. Adv. Atmos. Sci. 40, 393–409. https://doi.org/10.1007/s00376-022-2048-8.

von Luxburg, U., 2007. A tutorial on spectral clustering. Stat. Comput. 17, 395–416. https://doi.org/10.1007/s11222-007-9033-z.

Ma, X., Yang, B., Dai, G., Lin, H., Yang, X., Qian, Y., Zhang, Y., Huang, A., 2024. Contrasting effects of urban land cover change and anthropogenic heat on summer precipitation over the Yangtze River Delta of China: analyses from an atmospheric moisture budget perspective. J. Geophys. Res.-Atmos. 129, 18. https://doi.org/10.1029/2023jd039430.

Ma, Y., Hu, Z., Li, C., Feng, T., Meng, X., Dong, W., 2023. Anthropogenic climate change enhances the July 2021 super-heavy rainfall event in Central China. Bull. Am. Meteorol. Soc. 104, E736–E741. https://doi.org/10.1175/bams-d-22-0141.1.

Muñoz-Sabater, J., Dutra, E., Agustí-Panareda, A., Albergel, C., Arduini, G., Balsamo, G., Boussetta, S., Choulga, M., Harrigan, S., Hersbach, H., Martens, B., Miralles, D.G., Piles, M., Rodríguez-Fernández, N.J., Zsoter, E., Buontempo, C., Thépaut, J.N., 2021. ERA5-Land: a state-of-the-art global reanalysis dataset for land applications. Earth Syst. Sci. Data. 13, 4349–4383. https://doi.org/10.5194/essd-13-4349-2021.

Nakanishi, M., Niino, H., 2006. An improved mellor-yamada level-3 model: its numerical stability and application to a regional prediction of advection fog. Bound.-Layer Meteor. 119, 397–407. https://doi.org/10.1007/s10546-005-9030-8.

Neiman, P.J., Ralph, F.M., White, A.B., Kingsmill, D.E., Persson, P.O.G., 2002. The statistical relationship between upslope flow and rainfall in California's coastal mountains: Observations during CALJET. Mon. Weather Rev. 130, 1468–1492. https://doi.org/10.1175/1520-0493(2002)130<1468:Tsrbuf>2.0.Co;2.

Ningombam, S.S., Larson, E.J.L., Indira, G., Madhavan, B.L., Khatri, P., 2024. Aerosol classification by application of machine learning spectral clustering algorithm. Atmos. Pollut. Res. 15, 102026. https://doi.org/10.1016/j.apr.2023.102026.

Niyogi, D., Pyle, P., Lei, M., Arya, S.P., Kishtawal, C.M., Shepherd, M., Chen, F., Wolfe, B., 2011. Urban modification of thunderstorms: an observational storm climatology and model case study for the Indianapolis Urban Region. J. Appl. Meteorol. Climatol. 50, 1129–1144. https://doi.org/10.1175/2010jamc1836.1.

Ntelekos, A.A., Smith, J.A., Donner, L., Fast, J.D., Gustafson Jr., W.I., Chapman, E.G., Krajewski, W.F., 2009. The effects of aerosols on intense convective precipitation in the northeastern United States. Q. J. R. Meteorol. Soc. 135, 1367–1391. https://doi.org/10.1002/qj.476.

Olson, J.B., Kenyon, J.S., Angevine, W.A., Brown, J.M., Pagowski, M., Sušelj, K., 2019. A Description of the MYNN-EDMF Scheme and the Coupling to Other Components in WRF–ARW. https://doi.org/10.25923/n9wm-be49.

Qian, Y., Chakraborty, T.C., Li, J., Li, D., He, C., Sarangi, C., Chen, F., Yang, X., Leung, L. R., 2022. Urbanization impact on regional climate and extreme weather: current understanding, uncertainties, and future research directions. Adv. Atmos. Sci. 39, 819–860. https://doi.org/10.1007/s00376-021-1371-9.

Rosenfeld, D., 2000. Suppression of rain and snow by urban and industrial air pollution. Science 287, 1793–1796. https://doi.org/10.1126/science.287.5459.1793.

Rotunno, R., Houze, R.A., 2007. Lessons on orographic precipitation from the mesoscale alpine programme. Q. J. R. Meteorol. Soc. 133, 811–830. https://doi.org/10.1002/qj.67.

Sato, T., 2013. Mechanism of orographic precipitation around the meghalaya plateau associated with intraseasonal oscillation and the diurnal cycle. Mon. Weather Rev. 141, 2451–2466. https://doi.org/10.1175/mwr-d-12-00321.1.

Seager, R., Naik, N., Vecchi, G.A., 2010. Thermodynamic and dynamic mechanisms for large-scale changes in the hydrological cycle in response to global warming. J. Clim. 23, 4651–4668. https://doi.org/10.1175/2010jcli3655.1.

Shem, W., Shepherd, M., 2009. On the impact of urbanization on summertime thunderstorms in Atlanta: two numerical model case studies. Atmos. Res. 92, 172–189. https://doi.org/10.1016/j.atmosres.2008.09.013.

Shen, Y., Yang, L., 2023. Divergent urban signatures in rainfall anomalies explained by pre-storm environment contrast. Geophys. Res. Lett. 50, 14. https://doi.org/10.1029/2022gl101658.

Skamarock, C., Klemp, B., Dudhia, J., Gill, O., Liu, Z., Berner, J., Wang, W., Powers, G., Duda, G., Barker, D.M., Huang, X., 2019. A Description of the Advanced Research WRF Model Version 4.

Tai, S.L., Liou, Y.C., Chang, S.F., Sun, J.Z., 2020. The heavy rainfall mechanism revealed by a terrain-resolving 4DVar data assimilation system-a case study. Mon. Weather Rev. 148, 2307–2330. https://doi.org/10.1175/MWR-D-19-0244.1.

Tang, Y., Huang, A., Wu, P., Huang, D., Xue, D., Wu, Y., 2021. Drivers of summer extreme precipitation events over East China. Geophys. Res. Lett. 48, 12. https://doi.org/10.1029/2021gl093670.

Tewari, M., Chen, F., Wang, W., Dudhia, J., Lemone, A., Mitchell, E., Ek, M.B., Gayno, G., Wegiel, W., Cuenca, R.H., 2004. Implementation and Verification of the Unified Noah Land-Surface Model in the WRF Model [Presentation].

Thielen, J., Wobrock, W., Gadian, A., Mestayer, P.G., Creutin, J.D., 2000. The possible influence of urban surfaces on rainfall development:: a sensitivity study in 2D in the meso-γ-scale. Atmos. Res. 54, 15–39. https://doi.org/10.1016/s0169-8095(00)00041-7.

Utsumi, N., Kim, H., Kanae, S., Oki, T., 2017. Relative contributions of weather systems to mean and extreme global precipitation. J. Geophys. Res.-Atmos. 122, 152–167. https://doi.org/10.1002/2016jd025222.

Waliser, D., Guan, B., 2017. Extreme winds and precipitation during landfall of atmospheric rivers. Nat. Geosci. 10, 179–U183. https://doi.org/10.1038/ngeo2894.

Wang, J., Chen, Y., Nie, J., Yan, Z., Zhai, P., Feng, J., 2022. On the role of anthropogenic warming and wetting in the July 2021 Henan record-shattering rainfall. Sci. Bull. 67, 2055–2059. https://doi.org/10.1016/j.scib.2022.09.011.

Wei, P., Xu, X., Xue, M., Zhang, C., Wang, Y., Zhao, K., Zhou, A., Zhang, S., Zhu, K., 2023. On the key dynamical processes supporting the 21.7 Zhengzhou record-breaking hourly rainfall in China. Adv. Atmos. Sci. 40, 337–349. https://doi.org/10.1007/s00376-022-2061-y.

Wernli, H., Paulat, M., Hagen, M., Frei, C., 2008. SAL-A novel quality measure for the verification of quantitative precipitation forecasts. Mon. Weather Rev. 136, 4470–4487. https://doi.org/10.1175/2008mwr2415.1.

Xie, P., Joyce, R., Wu, S., Yoo, S.-H., Yarosh, Y., Sun, F., Lin, R., Program, N.C., 2019. NOAA climate Data Record (CDR) of CPC morphing technique (CMORPH) high resolution global precipitation estimates, Version 1 [indicate subset]. NOAA Nation. Cent. Environ. Inform [dataset]. https://doi.org/10.25921/w9va-q159.

Xu, J., Li, R., Zhang, Q., Chen, Y., Liang, X., Gu, X., 2022. Extreme large-scale atmospheric circulation associated with the "21•7" Henan flood. Sci. China-Earth Sci. 65, 1847–1860. https://doi.org/10.1007/s11430-022-9975-0.

Xu, W.X., Zipser, E.J., Chen, Y.L., Liu, C.T., Liou, Y.C., Lee, W.C., Jou, B.J.D., 2012. An orography-associated extreme rainfall event during TiMREX: initiation, storm evolution, and maintenance. Mon. Weather Rev. 140, 2555–2574. https://doi.org/10.1175/MWR-D-11-00208.1.

Yan, Z., Wang, J., Xia, J., Feng, J., 2016. Review of recent studies of the climatic effects of urbanization in China. Adv. Clim. Chang. Res. 7, 154–168.

Yang, L., Li, Q., Yuan, H., Niu, Z., Wang, L., 2021. Impacts of urban canopy on two convective storms with contrasting synoptic conditions over Nanjing, China. J. Geophys. Res.-Atmos. 126, 28. https://doi.org/10.1029/2020jd034509.

Yao, J., Chen, Y., Guan, X., Zhao, Y., Chen, J., Mao, W., 2022. Recent climate and hydrological changes in a mountain-basin system in Xinjiang, China. Earth-Sci. Rev. 226, 21. https://doi.org/10.1016/j.earscirev.2022.103957.

Yao, X., Li, R., 2023. Progress in research of the July 2021 extreme precipitation event in Henan province, China. Acta Meteorol. Sin. 81, 853–865.

Yu, M., Miao, S., Li, Q., 2017. Synoptic analysis and urban signatures of a heavy rainfall on 7 August 2015 in Beijing. J. Geophys. Res.-Atmos. 122, 65–78. https://doi.org/10.1002/2016jd025420.

Zeng, J., Huang, A., Wu, P., Huang, D., Zhang, Y., Tang, J., Zhao, D., Yang, B., Chen, S., 2023. Typical synoptic patterns responsible for summer regional hourly extreme precipitation events over the Middle and lower Yangtze River Basin, China. Geophys. Res. Lett. 50, 10. https://doi.org/10.1029/2023gl104829.

Zhang, F., Zhang, Q.H., Sun, J.Z., 2021. Initiation of an elevated mesoscale convective system with the influence of complex Terrain during Meiyu season. J. Geophys. Res.-Atmos. 126. https://doi.org/10.1029/2020JD033416.

Zhang, Q., Li, R., Sun, J., Lu, F., Xu, J., Zhang, F., 2023. A Review of Research on the Record-breaking Precipitation Event in Henan Province, China, July 2021. Adv. Atmos. Sci. 40, 1485–1500. https://doi.org/10.1007/s00376-023-2360-y.

Zhang, S., Chen, Y., Luo, Y., Liu, B., Ren, G., Zhou, T., Martinez-Villalobos, C., Chang, M., 2022. Revealing the circulation pattern most conducive to precipitation extremes in Henan Province of North China. Geophys. Res. Lett. 49, 11. https://doi.org/10.1029/2022gl098034.

Zhang, Y., Miao, S., Dai, Y., Bornstein, R., 2017. Numerical simulation of urban land surface effects on summer convective rainfall under different UHI intensity in Beijing. J. Geophys. Res.-Atmos. 122, 7851–7868. https://doi.org/10.1002/2017jd026614.

Zhang, Z., Huang, A., Huang, D., Zhao, D., Zhang, Y., Gu, C., Chen, S., 2024. Understanding the formation mechanism of the "21.7" extreme heavy rainfall event in Henan, China from a climatic perspective. Trans. Atmos. Sci. 47, 681–700. https://doi.org/10.13878/j.cnki.dqkxxb.20240515001.

Zhao, Y., Chen, D., Li, J., Chen, D., Chang, Y., Li, J., Qin, R., 2020a. Enhancement of the summer extreme precipitation over North China by interactions between moisture convergence and topographic settings. Clim. Dyn. 54, 2713–2730. https://doi.org/10.1007/s00382-020-05139-z.

Zhao, Y., Huang, A., Kan, M., Dong, X., Yu, X., Wu, Y., Zhang, X., Cai, S., 2020b. Characteristics of Hourly extreme precipitation along the Yangtze River Basin, China during Warm Season. Sci. Rep. 10, 13. https://doi.org/10.1038/s41598-020-62535-5.

Zhou, X., Sun, J., Zhang, L., Chen, G., Cao, J., Ji, B., 2020. Classification characteristics of continuous extreme rainfall events in North China. Acta. Meteor. Sin. 78, 761–777. https://doi.org/10.11676/qxxb2020.052.